Chapter 6

Design of Time-Dependent Non-Reflecting Boundary Conditions: The Two-Dimensional Case

In the three-dimensional case, it is always possible to express high-order spherical Hankel functions appearing in the impedance coefficients of the Dirichlet-to-Neumann map in terms of the zero-order spherical Hankel function, see equation (5.8). It is this special property for the three-dimensional case which allows for the derivation of simple expressions for the non-reflecting boundary operators in terms of powers of the wavenumber. As a consequence, an exact inverse Fourier transform was readily obtained to yield time-dependent boundary conditions that are exact for the first N spherical harmonics. Using this procedure, two alternative local in time sequences of non-reflecting boundary conditions were obtained; a local in space version, and a nonlocal in space version.

In contrast, for the two-dimensional case it is not possible to express high-order cylindrical (integer) Hankel functions appearing in the exact Dirichlet-to-Neumann impedance relation solely in terms of the zero-order cylindrical Hankel function. While it is possible to obtain spatially local non-reflecting boundary conditions in the frequency domain that exactly represent the first N cylindrical wave harmonics (Givoli and Keller [1990]), time-dependent counterparts are not readily derived because of the difficulty in obtaining an exact inverse Fourier transform for the two-dimensional Hankel function. However by taking advantage of an asymptotic approximation for the two-dimensional Hankel function for large values of a non-dimensional wavenumber kR, where R is the radial distance to Γ_∞, an approximate localization of the exact impedance relation, i.e. the Dirichlet-to-Neumann mapping, can be obtained which has a simple inverse Fourier transform. The localization process follows by first recasting the exact solution for the exterior problem as a power series expansion, through a recurrence relation for the cylindrical Hankel functions in terms of the zero-order and first-order Hankel functions. By using a far-field approximation for large kR, an approximate asymptotic expansion is constructed in terms of negative powers of the wavenumber and the radial distance to the artificial boundary.

Following Bayliss and Turkel [1980,1982], a sequence of local (differential) operators are then derived which satisfy the first m terms in this asymptotic expansion. This can be considered as a way of matching the first m terms of an approximate solution for outgoing waves on Γ_∞. The operators in this sequence are of progressively higher order and provide increasing accuracy as more terms are matched in the expansion. These boundary operators have an inverse Fourier transform allowing a family of boundary conditions to be defined which are local in space and time.

6.1 Dirichlet-to-Neumann Map in the Frequency Domain

Consider the reduced wave equation (Helmholtz equation) in the exterior domain Ω_∞ with harmonic time dependence $e^{-i\omega t}$, and ω, the angular frequency, is real and positive:

$$\nabla^2\phi + k^2\phi = 0 \qquad \text{in } \Omega_\infty \tag{6.1}$$

$$\phi = \bar{\phi} \qquad \text{on } \Gamma_\infty \tag{6.2}$$

$$\lim_{r\to\infty} \sqrt{r}\left(\frac{\partial\phi}{\partial r} - ik\phi\right) = 0 \tag{6.3}$$

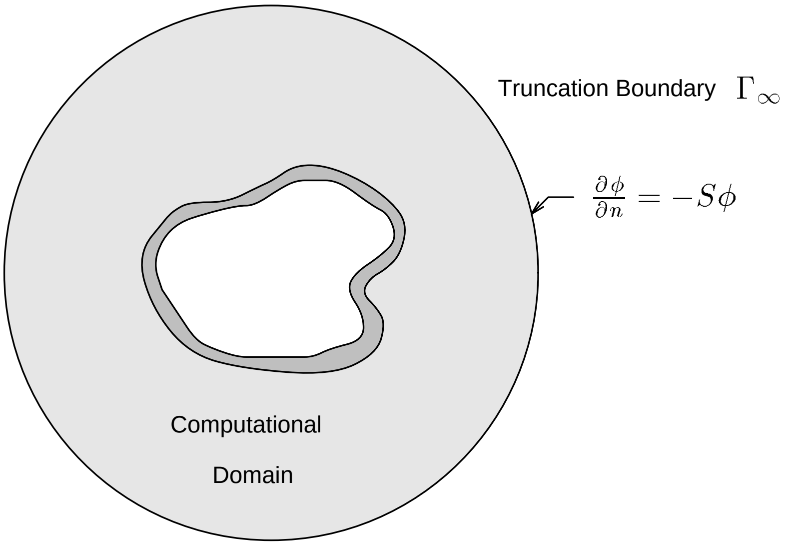

Figure 6.1: Illustration of a circular artificial boundary Γ_∞, enclosing the finite computational domain in $\mathrm{x} \in \mathbb{R}^2$.

where $k = \omega/c \geq 0$ is the acoustic wavenumber and $\bar{\phi}$ is the restriction of ϕ to Γ_∞. Equation (6.3) is the Sommerfeld radiation condition, (Sommerfeld [1964]) for the two-dimensional problem. This condition states that for a unique solution to the exterior problem, all waves at infinity must be outgoing. Restricting the artificial boundary Γ_∞ to be of separable geometry, in this case a circle of radius $r = R$ in two-dimensions (see Figure 6.1), we are able to express the general solution to this problem as an infinite series of cylindrical wave harmonics:

$$\phi(r,\theta) = \sum_{n=0}^{\infty} H_n(kr)(a_n \cos n\theta + b_n \sin n\theta) \qquad r \geq R \tag{6.4}$$

where for outgoing waves, $H_n(kr)$ are cylindrical Hankel functions of the first kind of order n. The function $\bar{\phi}(\theta)$ in (6.2) can be expanded in a Fourier series in the circumferential coordinate θ, and after equating its Fourier coefficients with (6.4) evaluated at $r = R$, i.e. setting $\phi(R,\theta) = \bar{\phi}(\theta)$, we obtain the two-dimensional solution,

$$\phi(r,\theta) = \sum_{n=0}^{\infty} \frac{H_n(kr)}{H_n(kR)} \alpha_n(\theta) \tag{6.5}$$

where

$$\alpha_n(\theta) = \frac{\varepsilon_n}{\pi} \int_0^{2\pi} \cos n(\theta - \theta') \; \phi(R, \theta') \; d\theta'$$

and $\varepsilon_0 = 1/2$ and $\varepsilon_n = 1, n \geq 1$.

Differentiating (6.5) with respect to r evaluated at $r = R$ results in the exact Dirchlet-to-Neumann (DtN) boundary condition in the frequency domain, see Keller and Givoli [1989].

$$\boxed{\frac{\partial \phi}{\partial n}(R, \theta) = \int_0^{2\pi} s_n(\theta - \theta') \; \phi(R, \theta') \; R \; d\theta'} \tag{6.6}$$

where

$$s_n(\theta - \theta') = \frac{\varepsilon_n \; k}{\pi R} \sum_{n=0}^{\infty} \frac{H_n'(kR)}{H_n(kR)} \cos n(\theta - \theta')$$

and $0 \leq \theta < 2\pi$ is the polar angle, and R is the radius of the circular truncation boundary Γ_∞. Eq. (6.6) can be written in operator form as,

$$\frac{\partial \phi}{\partial n} \quad = \quad -\mathbb{S} \; \phi \qquad \text{on } \Gamma_\infty \tag{6.7}$$

which represents a relation between Dirichlet and Neumann data through the linear operator $\mathbb{S}$. The DtN map $\mathbb{S}$, represents the exact impedance for the exterior acoustic fluid restricted to the artificial boundary. Furthermore, the operator $\mathbb{S}$ is an integral operator coupling all points on the artificial boundary Γ_∞, resulting in a nonlocal boundary condition. The direct time-dependent counterpart to this condition involves a convolution integral over time. As a result of the time integral, the boundary condition is nonlocal in time, requiring the storage of a large pool of historical data for long time solutions.

6.2 Local Boundary Operators in the Frequency Domain

For the two-dimensional case, it is not possible to express high-order cylindrical Hankel functions $H_n(kR)$, solely in terms of the zero-order function $H_0(kR)$ as was done for the three-dimensional case; see Watson [1966] for the definition of the cylindrical

Hankel functions $H_n(kR)$ as an infinite series involving the argument kR and the order n. While it is possible to obtain spatially local non-reflecting boundary conditions in the frequency domain that exactly represent the first N cylindrical wave harmonics (Givoli and Keller [1990]), time-dependent counterparts are not readily obtained do to the difficulty in obtaining an exact inverse Fourier transform for the two-dimensional Hankel function. To address this difficulty, we construct approximate boundary conditions which are local in both space and time by expressing the exact solution (6.5) in an alternative form. To this end, we use the recurrence formula for Hankel functions to express $H_n(kr)$ in (6.5) as a linear combination of $H_0(kr)$ and $H_1(kr)$, see Watson [1966]:

$$H_n(kr) = P_n H_0(kr) + Q_n H_1(kr) \tag{6.8}$$

where $P_n(1/kr)$ and $Q_n(1/kr)$ are Lommel's polynomials of degree n in the variable $1/kr$. The polynomials can be obtained recursively as,

$$P_n = \frac{2(n-1)}{kr} P_{n-1} - P_{n-2} \tag{6.9}$$

$$Q_n = \frac{2(n-1)}{kr} Q_{n-1} - Q_{n-2} \tag{6.10}$$

with starting values $P_0 = 1,\ P_1 = 0,\ Q_0 = 0,\ Q_1 = 1$. The resulting expression, namely

$$\phi(r,\theta) = H_0(kr) \sum_{n=0}^{\infty} P_n \frac{\alpha_n(\theta)}{H_n(kR)} + H_1(kr) \sum_{n=0}^{\infty} Q_n \frac{\alpha_n(\theta)}{H_n(kR)} \tag{6.11}$$

can be rearranged to take the form of an asymptotic expansion in $1/kr$:

$$\phi(r,\theta) = H_0(kr) \sum_{j=0}^{\infty} \frac{F_j(\theta)}{(kr)^j} + H_1(kr) \sum_{j=0}^{\infty} \frac{G_j(\theta)}{(kr)^j} \tag{6.12}$$

This series is uniformly and absolutely convergent and can be differentiated termwise with respect to r any number of times, see Karp [1961]. Interestingly, $F_0(\theta)$ contains only even-numbered coefficients, and $G_0(\theta)$ contains only odd ones:

$$F_0(\theta) = \sum_{n=0}^{\infty} \frac{(-1)^{n/2}}{H_n(kR)} \frac{\varepsilon_n}{\pi} \int_0^{2\pi} \cos n(\theta-\theta')\ \phi(R,\theta')\ d\theta' \qquad n = 0, 2, 4, \cdots$$

$$G_0(\theta) \quad = \quad \sum_{n=1}^{\infty} \frac{(-1)^{(n-1)/2}}{H_n(kR)} \frac{\varepsilon_n}{\pi} \int_0^{2\pi} \cos n(\theta - \theta')\ \phi(R, \theta')\ d\theta' \quad n = 1, 3, 5, \cdots$$

The coefficients $F_j(\theta)$ and $G_j(\theta)$ can be obtained recursively in terms of F_0 and G_0. They are nonlocal functions, and if evaluated explicitly would lead to an exact boundary condition. Here a method of eliminating this source of non-locality is described.

We first introduce the asymptotic expansion of the Hankel functions, for large kr, see WATSON [1966]:

$$H_n(kr) = (-i)^n \sqrt{\frac{2}{\pi kr}} e^{i(kr - \pi/4)} \left\{ 1 - \frac{(4n^2 - 1)}{8ikr} + \mathcal{O}\left((kr)^{-2}\right) \right\} \tag{6.13}$$

After substituting this approximation for $H_0(kr)$ and $H_1(kr)$ into (6.12) and accepting an error of the order $\mathcal{O}\left((kr)^{-3/2}\right)$ an approximate asymptotic expansion is obtained:

$$\boxed{\phi(r, \theta) \sim \hat{\phi}(r, \theta) = \sqrt{\frac{2}{\pi kr}} e^{i(kr - \pi/4)} \sum_{j=0}^{\infty} \frac{f_j(\theta)}{(kr)^j}} \tag{6.14}$$

where

$$f_0(\theta) = F_0(\theta) - i\ G_0(\theta) = \sum_{n=0}^{\infty} \frac{(-i)^n}{H_n(kR)} \frac{\varepsilon_n}{\pi} \int_0^{2\pi} \cos n(\theta - \theta')\ \phi(R, \theta')\ d\theta'$$

The coefficients $f_j(\theta)$ can be obtain recursively in terms of f_0.

Following BAYLISS AND TURKEL [1980,1992], a sequence of local differential operators which eliminate the first m nonlocal terms $f_j(\theta)$ in this asymptotic expansion is found. Splitting the asymptotic series (6.14) into two sums and multiplying by $r^{m-1/2}$ throughout, we obtain

$$r^{m-1/2} \hat{\phi} = e^{ikr} \sum_{j=1}^{m} r^{m-j} g_j(\theta) + e^{ikr} \sum_{j=m+1}^{\infty} r^{m-j} g_j(\theta) \tag{6.15}$$

where we have regrouped the coefficients as

$$g_j(\theta) = \sqrt{\frac{2}{\pi}} e^{-i\pi/4} f_{j-1}(\theta) k^{1/2-j}$$

Applying the local differential operator

$$L_o = \frac{\partial}{\partial r} - ik \tag{6.16}$$

to the power of m, i.e. $(L_o)^m$ to both sides of (6.15), the first sum is annihilated. In order to obtain a sequence of operators acting only on $\hat{\phi}$, we write explicitly for $m = 1$ and $m = 2$,

$$\begin{aligned} B_1\hat{\phi} &= L_o^1(r^{1/2}\hat{\phi})/r^{1/2} = (L_o + 1/2r)\hat{\phi} \\ B_2\hat{\phi} &= L_o^2(r^{3/2}\hat{\phi})/r^{3/2} = (L_o + 5/2r)(L_o + 1/2r)\hat{\phi} \end{aligned}$$

By analogy, the local operators are defined recursively as,

$$B_m = \prod_{j=1}^{m} (L_j) = L_m \; L_{m-1} \cdots L_2 \; L_1 \tag{6.17}$$

where

$$L_j = \left(\frac{\partial}{\partial r} - ik + \frac{2j - 3/2}{r} \right), \quad j = 1, 2, \cdots m \tag{6.18}$$

The B_m operator matches the first m terms in the expansion (6.14) with a remainder of order,

$$\begin{aligned} B_m\hat{\phi} &= \prod_{j=1}^{m} (L_j) \cdot \sqrt{\frac{2}{\pi kr}} e^{i(kr-\pi/4)} \sum_{j=1}^{\infty} \frac{f_{j-1}(\theta)}{(kr)^{j-1}} \\ &= \prod_{j=1}^{m} (L_j) \cdot \sqrt{\frac{2}{\pi kr}} e^{i(kr-\pi/4)} \sum_{j=m+1}^{\infty} \frac{f_{j-1}(\theta)}{(kr)^{j-1}} \\ &= \mathcal{O}\left(r^{-m}(kr)^{-m-1/2}\right) \end{aligned} \tag{6.19}$$

Remarks

1. Observe the character of the result (6.19) for fixed kr with increasing m, i.e, $\lim_{m\to\infty} B_m(\phi) = 0$ Thus we define as a hierarchical family of approximate boundary conditions on the artificial boundary,

$$B_m(\phi) := 0 \qquad \text{on} \;\; \Gamma_\infty \tag{6.20}$$

These are higher order boundary conditions on Γ_∞ and provide increasing accuracy with m, allowing in principle the computational region to be reduced to a minimum.

2. The accuracy of these local operators also depends strongly on the parameter kr such that for a fixed r,

$$\lim_{k\to\infty} B_m(\phi) = 0 \tag{6.21}$$

In this way, the B_m operators can be viewed as high frequency approximations of increasing order. From this property the local non-reflecting boundary conditions are increasingly accurate as the frequency (wavenumber) is increased relative to the dimension of the radiator/scatterer.

3. On the other hand, it is expected that the operators will be increasingly accurate as the position of the artificial boundary $r = R$, approaches infinity, i.e.,

$$\lim_{r\to\infty} B_m(\phi) = 0 \tag{6.22}$$

4. The well known plane-wave (PW) differential operator

$$L_o\phi = \left(\frac{\partial}{\partial r} - ik\right)\phi = \mathcal{O}(1/r(kr)^{1/2}) \tag{6.23}$$

is exact in one-dimension, however in higher dimensions, it is generally very inaccurate except at very high frequencies (short wavelength) or at large r. In fact, it can easily be seen that it does not even annihilate the first term in the expansion (6.14).

5. The sequence of operators B_m can be viewed as extensions of the plane-wave approximation. Indeed, we note that the first boundary operator B_1 in the sequence coincides with the cylindrical damper or curved wave approximation.

$$B_1\phi = \left(\frac{\partial}{\partial r} + \frac{1}{2r} - ik\right)\phi \tag{6.24}$$

As $r \to \infty$, the B_1 operator reduces to the PW radiation condition L_o.

6.3 Local Boundary Operators in the Time Domain

Time-dependent operators are obtained by applying an inverse Fourier transform to the time-harmonic operators defined in (6.17). In effect, replacing every occurrence of the operator $-ik$ by $\frac{1}{c}\frac{\partial}{\partial t}$ with the result,

$$\boxed{B_m = \prod_{j=1}^{m} \left(\frac{\partial}{\partial r} + \frac{1}{c}\frac{\partial}{\partial t} + \frac{2j - 3/2}{r} \right)} \tag{6.25}$$

The sequence of operators B_m provides increasing accuracy with m which, however, is also a measure of the difficulty of implementation. The operator B_m involves m^{th} order partial derivatives with respect to r and time t. High order radial partial derivatives are not desirable in the context of finite element analysis because of the implied higher order continuity condition between elements. For $m \geq 2$, the order of differentiation cannot be conveniently reduced to $C^o(\Gamma_\infty)$ by integration-by-parts in the weak form. However, all radial derivatives beyond the first can be eliminated in favor of tangential and time derivatives by the recursive use of the wave equation in polar coordinates:

$$\frac{\partial^2 \phi}{\partial r^2} + \frac{1}{r}\frac{\partial \phi}{\partial r} + \frac{1}{r^2}\Delta_\Gamma \phi - \frac{1}{c^2}\frac{\partial^2 \phi}{\partial t^2} = 0, \tag{6.26}$$

where $\Delta_\Gamma = \partial^2 \ /\partial\theta^2$ is the Laplace-Beltrami operator in two-dimensions.
For example consider the B_2 operator,

$$B_2\phi = \frac{\partial^2 \phi}{\partial r^2} + \frac{2}{c}\frac{\partial^2 \phi}{\partial r \partial t} + \frac{1}{c^2}\frac{\partial^2 \phi}{\partial t^2} + \frac{3}{rc}\frac{\partial \phi}{\partial t} + \frac{3}{r}\frac{\partial \phi}{\partial r} + \frac{3\phi}{4r^2} \tag{6.27}$$

$\partial^2\phi/\partial r^2$ can now be eliminated by use of (6.26), to arrive at a form with only first order radial derivatives.

$$\boxed{B_2 = \frac{1}{r}\frac{\partial}{\partial r} + \frac{1}{c}\frac{\partial^2}{\partial r \partial t} - \left(\frac{1}{2r^2}\right)\Delta_\Gamma + \frac{3}{8r^2} + \frac{3}{2rc}\frac{\partial}{\partial t} + \frac{1}{c^2}\frac{\partial^2}{\partial t^2}} \tag{6.28}$$

Note that the boundary operators are local in both space and time, i.e., they are differential operators. As a consequence, when used in a semidiscrete finite element method, the resulting equations form a mth order system of ordinary differential equations in time. For orders $m \leq 2$, standard time-stepping schemes can be used to solve the resulting system directly, see Chapter 7. However for $m \geq 3$, the boundary operators involve time derivatives up to the mth order, and special time-integrators must be developed. From this observation, it appears that a time-discontinuous space-time formulation may be the only practical way of implementing higher-order boundary conditions of this form beyond second-order.

6.4 Space-Time Finite Element Implementation

After elimination of higher order radial derivatives and restricting the artificial boundary to be a circle, we define the operators $\mathbb{S}_m$ in (2.33) as,

$$B_m(\phi) \equiv \frac{\partial \phi}{\partial n} + \mathbb{S}_m\ \phi \qquad \text{on} \ \ \Gamma_\infty \tag{6.29}$$

which implies

$$\nabla \phi \cdot \boldsymbol{n} \quad = \quad -\mathbb{S}_m\ \phi \qquad \text{on} \ \ \Gamma_\infty \tag{6.30}$$

which is in the form of a local, (i.e. differential) Dirichlet to Neumann boundary condition through the map $\mathbb{S}_m$. We identify the first two operators $\mathbb{S}_m$ for m equal to 1 and 2 as:

$$\mathbb{S}_1\ \phi \quad = \quad \frac{1}{2R}\phi + \frac{1}{c}\dot{\phi} \tag{6.31}$$

$$\mathbb{S}_2\ \phi \quad = \quad \frac{1}{2R}(3/4 - \frac{\partial^2}{\partial \theta^2})\phi + \frac{3}{2c}\dot{\phi} + \frac{R}{c}\frac{\partial \dot{\phi}}{\partial r} + \frac{R}{c^2}\ddot{\phi} \tag{6.32}$$

These boundary conditions are incorporated into the finite element method as natural boundary conditions, i.e., they are enforced weakly in space-time.

For $\mathbb{S}_2$, the acoustic intensity operator defined in (3.33) specializes to,

$$d_0(\dot{w}^h\ ,\ \phi^h)_{(\Upsilon_\infty)_n} \quad = \quad \frac{3}{8R}(\dot{w}^h\ ,\ \phi^h)_{(\Upsilon_\infty)_n} + \frac{1}{2R}(\dot{w}^h_{,\theta}\ ,\ \phi^h_{,\theta})_{(\Upsilon_\infty)_n} \tag{6.33}$$

$$d_1(\dot{w}^h\ ,\ \dot{\phi}^h)_{(\Upsilon_\infty)_n} \quad = \quad \frac{3}{2c}(\dot{w}^h\ ,\ \dot{\phi}^h)_{(\Upsilon_\infty)_n} + \frac{R}{c}(\dot{w}^h\ ,\ \dot{\phi}^h_{,r})_{(\Upsilon_\infty)_n} \tag{6.34}$$

$$d_2(\dot{w}^h\,,\,\ddot{\phi}^h)_{(\Upsilon_\infty)_n} \;=\; \frac{R}{c^2}(\dot{w}^h\,,\,\ddot{\phi}^h)_{(\Upsilon_\infty)_n} \tag{6.35}$$

Continuity requirements due to second-order tangential derivatives $\partial^2/\partial\theta^2$, are relaxed on the artificial boundary Γ_∞, by the use of the identity,

$$(w\,,\,\phi_{,\theta\theta})_{\Gamma_\infty} = -(w_{,\theta}\,,\,\phi_{,\theta})_{\Gamma_\infty} \tag{6.36}$$

Since these boundary operators are local in space and time, they preserve the sparse banded data structure of the finite element arrays. Analogous to the three-dimensional case, the second term in the expression for d_1 contains a spatially nonsymmetric contribution localized to the artificial boundary Γ_∞.

Recall that at Γ_∞, temporal continuity is weakly enforced across space-time slabs through temporal jump operators embedded in the operators $d_2(\cdot\,,\,\cdot)_{\Gamma_\infty}$ and $d_0(\cdot\,,\,\cdot)_{\Gamma_\infty}$, see (3.26). For $\mathbb{S}_2$, the consistent jump terms are,

$$\begin{aligned} d_0(w^h(t_n^+)\,,\,[\![\phi^h(t_n)]\!])_{\Gamma_\infty} \;&=\; \frac{3}{8R}(w^h(t_n^+)\,,\,[\![\phi^h(t_n)]\!])_{\Gamma_\infty} \\ &+\; \frac{1}{2R}(w^h_{,\theta}(t_n^+)\,,\,[\![\phi^h_{,\theta}(t_n)]\!])_{\Gamma_\infty} \end{aligned} \tag{6.37}$$

$$d_2(\dot{w}^h(t_n^+)\,,\,[\![\dot{\phi}^h(t_n)]\!])_{\Gamma_\infty} \;=\; \frac{R}{c^2}(\dot{w}^h(t_n^+)\,,\,[\![\dot{\phi}^h(t_n)]\!])_{\Gamma_\infty} \tag{6.38}$$

6.5 Numerical Examples: Radiation

In this section several two-dimensional numerical examples are solved to demonstrate the effectiveness of the time-discontinuous Galerkin space-time finite element method to accurately model time-dependent acoustic radiation. The problems studied are primarily designed to assess the performance of the two-dimensional, local non-reflecting boundary conditions when implemented in the space-time formulation. For all the numerical results presented, the GLS mesh parameters were set to zero and quadratic space-time finite elements were used throughout.

6.5.1 Circumferential harmonic radiation

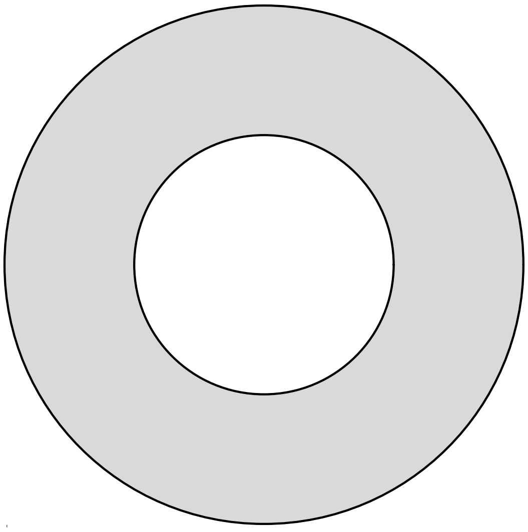

Figure 6.2: Circular cylinder of radius $r = a$, enclosed by a circular artificial boundary of radius $R = 2a$.

In this example we study the uncoupled problem of an infinite circular cylinder of radius $a = 1$, with circumferentially harmonic radiation loading,

$$\phi(a, \theta, t) = \cos n\theta \sin \omega t \qquad \text{for } 0 \leq \theta < 2\pi\,, \quad t > 0 \tag{6.39}$$

The exact steady-state solution for this problem is for $r \geq a$,

$$\phi(r, \theta, t) = -\mathrm{Imag}\left\{ \frac{H_n(kr)}{H_n(ka)} \cos n\theta \mathrm{e}^{-i\omega t} \right\} \tag{6.40}$$

where H_n are cylindrical Hankel functions of the first kind of order n. When using a finite element method incorporating approximate non-reflecting boundary conditions on a circular artificial boundary as illustrated in Figure 6.2, this problem becomes increasingly difficult to solve as the circumferential harmonic n increases. It is expected that as the mode n is increased and the radiation pattern becomes more complex, the higher-order operators $\mathbb{S}_m$ will be increasingly accurate compared to the simple PW damper, denoted $\mathbb{S}_0$.

Taking advantage of the symmetry in this problem, the computational domain is taken as, $\Omega = \{a < r < R,\ 0 \leq \theta < \pi\}$, where the truncation boundary is set at $R = 2a$ and Ω is discretized with 10 elements in the radial direction, and 40 elements

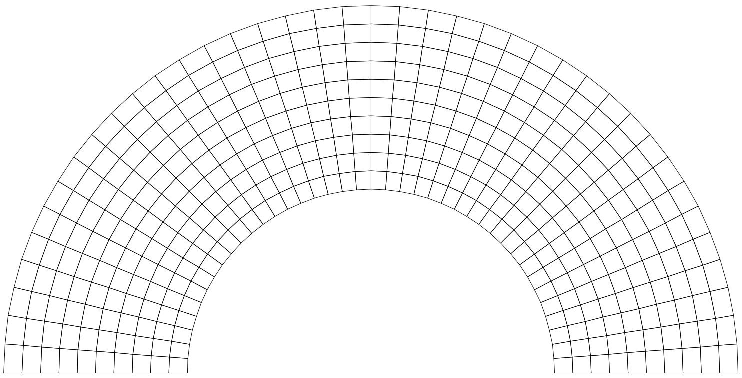

Figure 6.3: Finite element mesh for the radiating circular cylinder: By symmetry, only the upper half is discretized with 400 quadratic elements.

in the polar direction; see Figure 6.3. A series of transient space-time finite element solutions were obtained for this two-dimensional problem using zero initial conditions on ϕ and $\dot{\phi}$ and a time-increment of $\Delta t = 0.1$.

Harmonic $n = 0$:

In order to study the accuracy of the boundary operator $\mathbb{S}_1$ to transmit uniform acoustic radiation, we set $n = 0$, resulting in the 'breathing' mode $\phi(a,t) = \sin \omega t$. An exact local radiation condition on a circular boundary Γ_∞ can be obtained for this simple case of uniform radiation in the frequency domain by setting $n = 0$ in (6.4), differentiating with respect to r and evaluating the result at $r = R$.

$$\frac{\partial \phi}{\partial r} = -k \frac{H_1(kR)}{H_0(kR)} \phi \qquad \text{at} \quad r = R \tag{6.41}$$

As this boundary condition involves the cylindrical Hankel function, its exact time-dependent counterpart cannot be readily obtained. However by using the asymptotic representation of $H_0(kr)$ as $kr \to \infty$ given in (6.13), the asymptotic solution to this

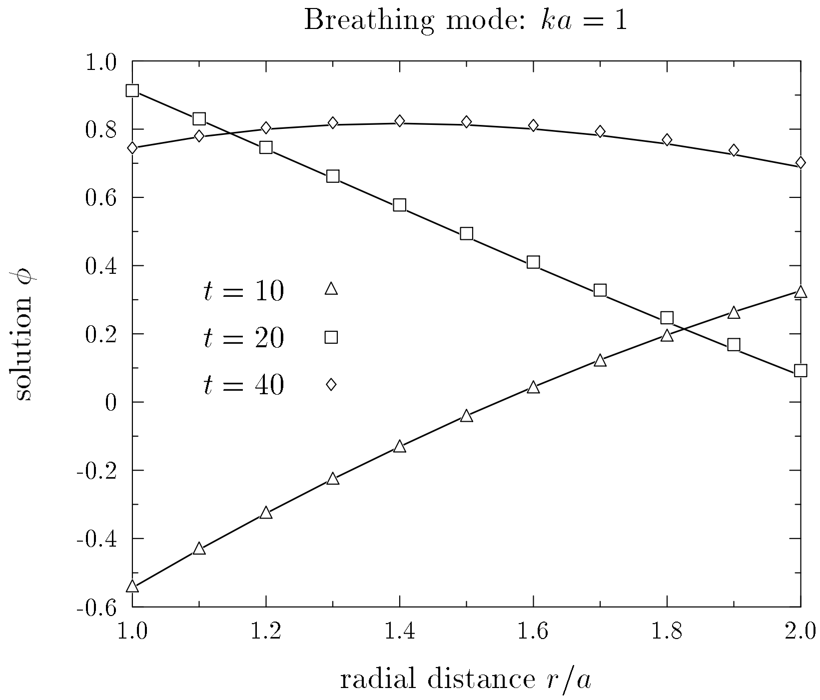

Figure 6.4: Breathing mode ($n = 0$) for circular cylinder with $ka = 1$. Solution using S_1 local boundary condition; profile along the radial distance $a < r < R$, at times $t = 10, 20, 40$.

problem becomes,

$$\phi(r,t) \sim \tilde{\phi} = \frac{1}{H_0(ka)}\sqrt{\frac{2}{\pi kr}}e^{ik((r-\pi/4)-ct)} \qquad \text{for } kr \to \infty \tag{6.42}$$

The nature of the cylindrical wave motion is evident from this asymptotic solution; it reduces to a spreading wave with a $(1/\sqrt{r})$ amplitude decay in the far field, while the wave field near the cylinder is relatively complex. Differentiating with respect to r and taking an inverse Fourier transform we obtain,

$$\frac{\partial\tilde{\phi}}{\partial r} = \left(-\frac{1}{c}\frac{\partial}{\partial t} - \frac{1}{2R}\right)\tilde{\phi} \qquad \text{at} \quad r = R \tag{6.43}$$

This local condition is identical to the B_1 operator defined in (6.25) and is asymptotically convergent to the exact solution for large kr:

$$B_1(\tilde{\phi}) = \left(\frac{\partial}{\partial r} + \frac{1}{c}\frac{\partial}{\partial t} + \frac{1}{2r}\right)\tilde{\phi} = 0 \tag{6.44}$$

This conclusion is also valid for any higher order local boundary operator, (B_m, $m \geq 2$), i.e.

$$B_m(\tilde{\phi}) = \prod_{j=2}^{m}(L_j) \cdot B_1(\tilde{\phi}) = \prod_{j=2}^{m}(L_j) \cdot 0 = 0 \qquad \text{for } m \geq 2 \tag{6.45}$$

where the definition of the differential operators L_j are defined in (6.18). We expect the operators (B_m, $m \geq 2$) to add no additional increase in accuracy for this special case involving uniform cylindrical waves.

Figure 6.4 shows the profile of the transient space-time finite element solution for $ka = 1$ along the radial coordinate at three sample times. The solution sample times are chosen such that many spurious reflections between the artificial boundary and the cylinder could have occurred. From these results it is observed that the operator $\mathbb{S}_1$, when implemented in the discontinuous Galerkin formulation gives very accurate solutions for the cylindrical 'breathing' ($n = 0$) mode as expected. As the normalized frequency ka, is increased, it is observed that the solution becomes increasingly accurate.

Harmonic $n = 1$:

In this example, the accuracy of the second-order boundary operator $\mathbb{S}_2$ in transmitting waves corresponding to harmonic $n = 1$, is studied. Figure 6.5 illustrates the contours of the discontinuous Galerkin solution for $ka = 1$ and incorporating the 'plane-wave' boundary operator, denoted $\mathbb{S}_0$, the first-order, $\mathbb{S}_1$ and second-order $\mathbb{S}_2$ boundary operators defined in (6.31) and (6.32). Figure 6.6 shows the solution profile around the artificial boundary and the solution plotted along a radial line located at the angle $\theta = 0$, at time $t = 30$. Results confirm that the local operator $\mathbb{S}_2$, when implemented in the space-time formulation, gives accurate solutions while solutions using either $\mathbb{S}_0$ or $\mathbb{S}_1$ have significant error.

Harmonic $n = 2$:

As the harmonic loading is increased to $n = 2$, the acoustic radiation pattern becomes more complex. For a driving frequency $ka = 1$, significant errors occur in the solution using $\mathbb{S}_0$ or $\mathbb{S}_1$, while the solution using $\mathbb{S}_2$ remains accurate throughout the computational domain, see Figures 6.7 and 6.8 .

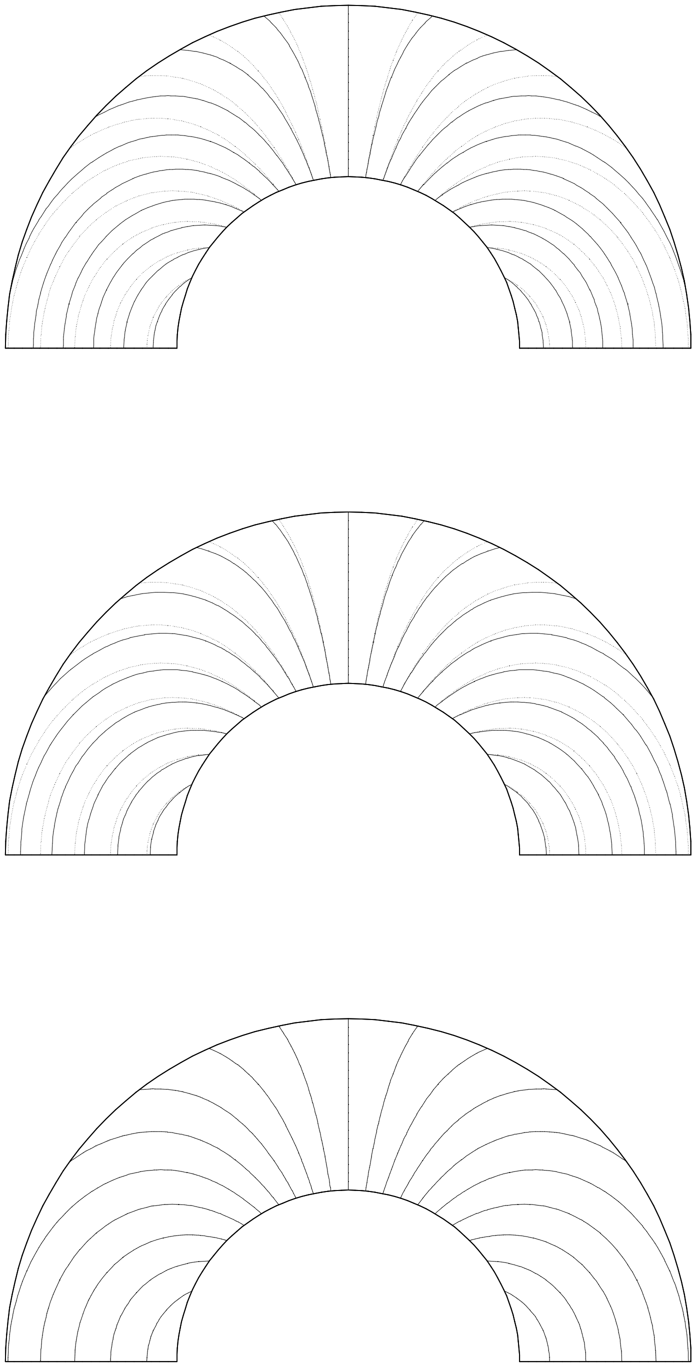

Figure 6.5: Radiation from a circular cylinder with circumferential harmonic $n = 1$, and normalized frequency $ka = 1$. Contours of space-time solution at time $t = 30$, using local boundary conditions, (Top): 'plane-wave' S_0, (Middle): first-order S_1, (Bottom): second-order S_2. (dotted contours denote analytical solution).

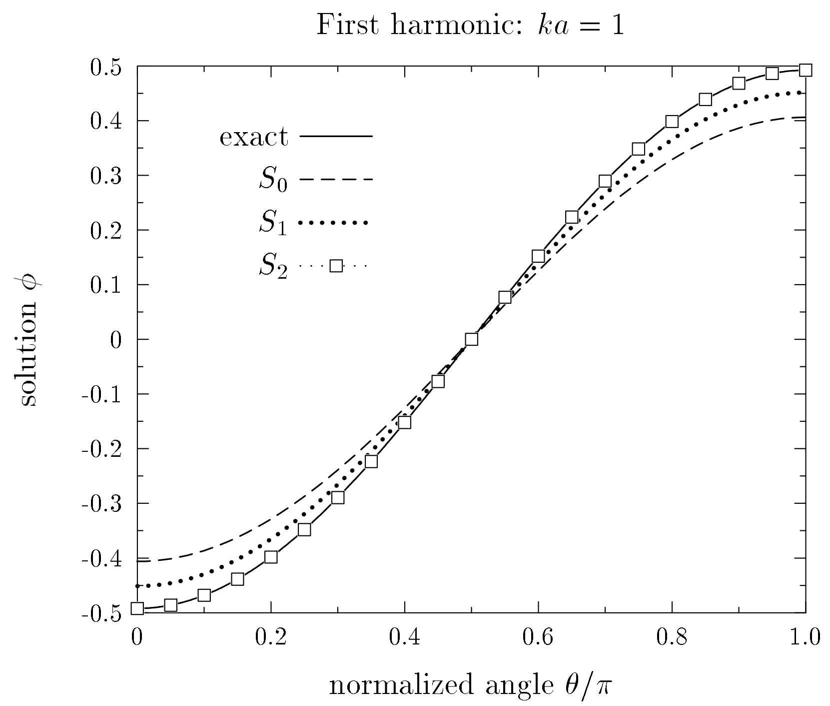

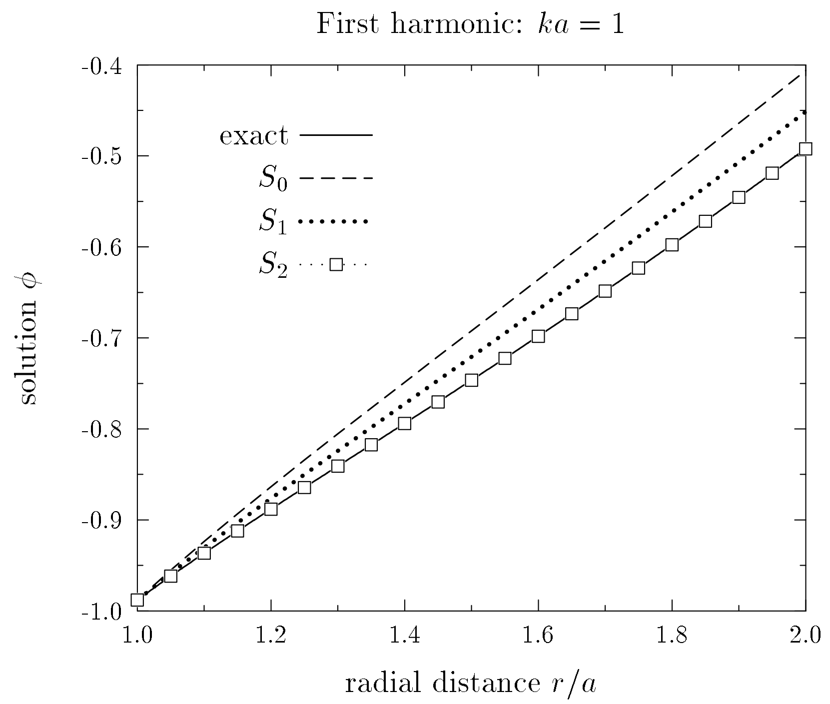

Figure 6.6: Circumferential wave harmonic $n = 1$: Results at $t = 30$, comparing the 'plane-wave' S_0, first-order S_1, and second-order S_2 boundary conditions. (Top): Solution profile on the artificial boundary $r = R$. (Bottom): Solution plotted along radial line at $\theta = 0$.

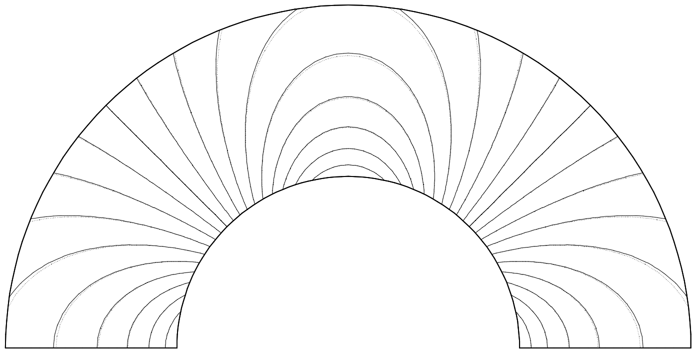

Figure 6.7: Radiation from a circular cylinder with circumferential harmonic $n = 2$, and normalized frequency $ka = 1$. Contours of space-time solution at time $t = 30$, using the second-order S_2 local boundary condition. (dotted contours denote analytical solution).

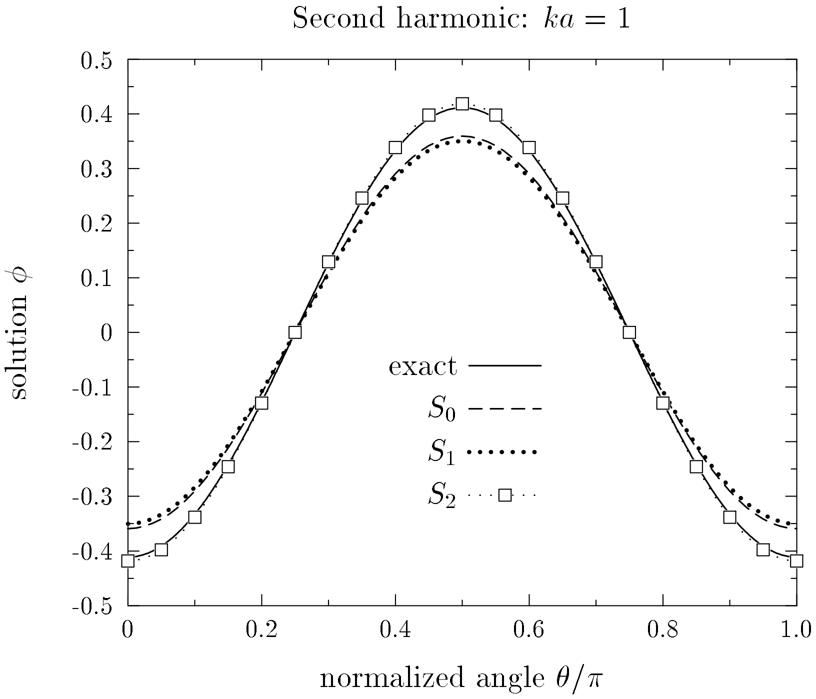

Figure 6.8: Circumferential wave harmonic $n = 2$: Results at $t = 30$, comparing the 'plane-wave' S_0, first-order S_1, and second-order S_2 boundary conditions. Solution profile on the artificial boundary $r = R$.

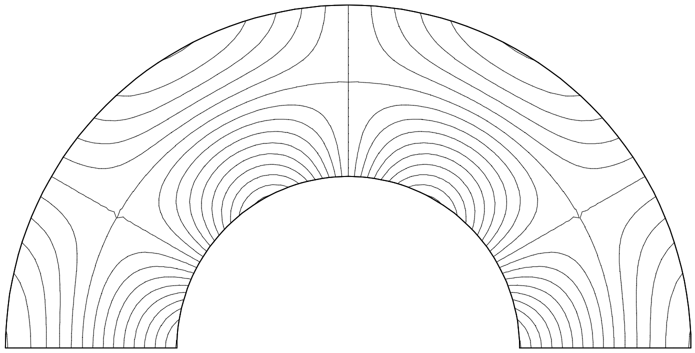

Figure 6.9: Radiation from a circular cylinder with circumferential harmonic $n = 3$, and normalized frequency $ka = 3$. Contours of space-time solution at time $t = 20$, using the second-order S_2 local boundary condition. (dotted contours denote analytical solution).

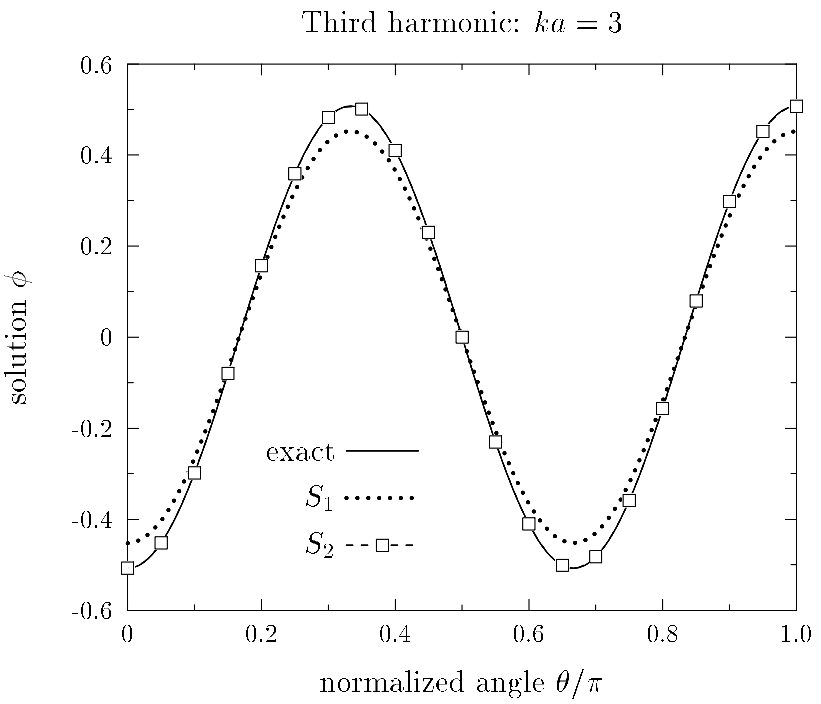

Figure 6.10: Circumferential wave harmonic $n = 3$: Results at $t = 20$, comparing the first-order S_1, and second-order S_2 boundary conditions. Solution profile on the artificial boundary $r = R$.

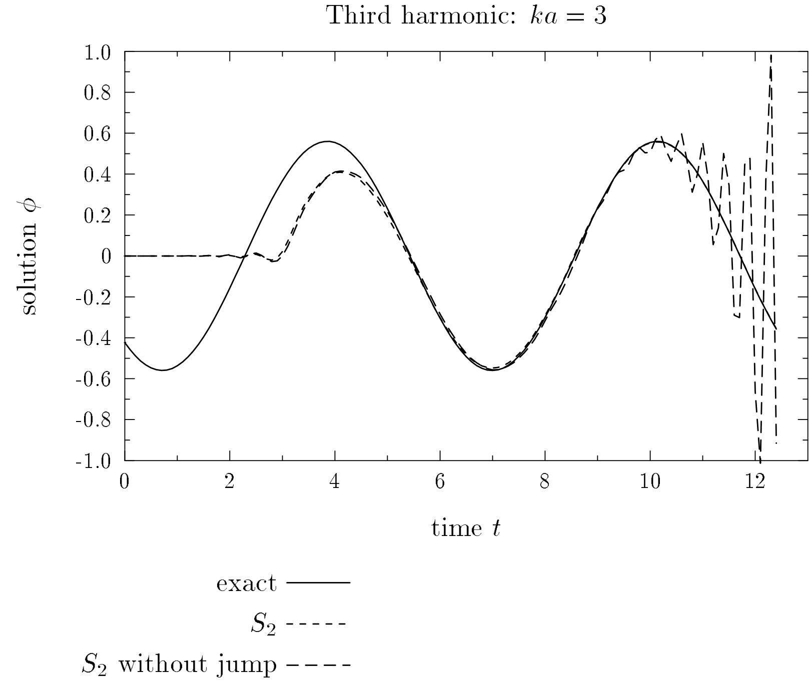

Figure 6.11: Illustration of stability: Radiating circular cylinder with loading $\cos 3\theta \sin \omega t$. Results at the artificial boundary Γ_∞, demonstrate that temporal jump terms are needed on Γ_∞ for stability.

Harmonic $n = 3$:

Numerical solutions for harmonic $n = 3$, with $ka = 1$ show significant error for all three local boundary operators tested. However by increasing the nondimensional wavenumber to $ka = 3$, accurate results are obtained for $\mathbb{S}_2$, see Figures 6.9 and 6.10. Results using $\mathbb{S}_1$ show significant error in the solution, while the solution using $\mathbb{S}_2$ is very accurate; with the numerical and analytical solutions almost indistinguishable. This example demonstrates how for a fixed distance R, and order m, the sequence of local boundary operators become increasingly accurate as the wavenumber is increased.

6.5.2 Illustration of Stability

Figure 6.11 illustrates the need for the weak enforcement of initial data between time slabs on the truncation boundary Γ_∞. The result shows the solution time-history for harmonic $n = 3$, on the truncation boundary at $(r\,,\,\theta) = (R\,,\,0)$. The solid line is the exact time-harmonic solution. When the consistent jump terms defined in (6.37) and

(6.38) are included, the local boundary condition, $\mathbb{S}_2$, displays the correct transient solution for short time, (time less than 6 seconds), and then quickly assumes the exact steady-state solution. When the temporal jump terms are omitted, i.e.

$$\begin{aligned} d_2(\dot{w}^h(t_n^+)\,,\, [\![\dot{\phi}^h(t_n)]\!])_{\Gamma_\infty} &= 0 \\ d_0(w^h(t_n^+)\,,\, [\![\phi^h(t_n)]\!])_{\Gamma_\infty} &= 0 \end{aligned}$$

then the solution quickly becomes unstable, generating large spurious oscillations, leading eventually to overflow. This example demonstrates how these additional operators are needed to ensure a stable solution, and are the key element that enable generalization of the time discontinuous Galerkin method to handle non-reflecting boundary conditions.

6.5.3 Radiation from a line element on a cylinder

To study the performance of the local non-reflecting boundary conditions for a challenging problem involving an infinite number of circumferential harmonics, consider the non-uniform radiation from a line element on an infinite circular cylinder of radius $r = a$, with loading

$$\phi(a, \theta, t) = \sin \omega t, \qquad \text{for } -\theta_p \le \theta \le \theta_p, \quad t > 0 \tag{6.46}$$

Elsewhere on the surface $r = a$, the solution vanishes. The steady-state analytical solution for this problem is,

$$\phi(r, \theta, t) = -\text{Imag}\left\{ \sum_{n=0}^{\infty} \frac{H_n(kr)}{H_n(ka)} \left[\frac{\epsilon_n \sin \theta_p}{n\pi} \right] \cos n\theta \, \mathrm{e}^{-i\omega t} \right\} \tag{6.47}$$

where $\epsilon_0 = 1/2$ and $\epsilon_n = 1, n \ge 1$ and H_n are Hankel functions of the first kind of order n. For low values of the normalized wavenumber ka, this solution is relatively uniform in the circumferential direction. The directionality of the solution grows as the wavenumber k is increased, and the solution becomes attenuated at the side of the cylinder opposite the radiating element.

In this example, the properties and discretization are unchanged from the previous problem. Figure 6.12 (top) shows the contours of the analytical series solution with

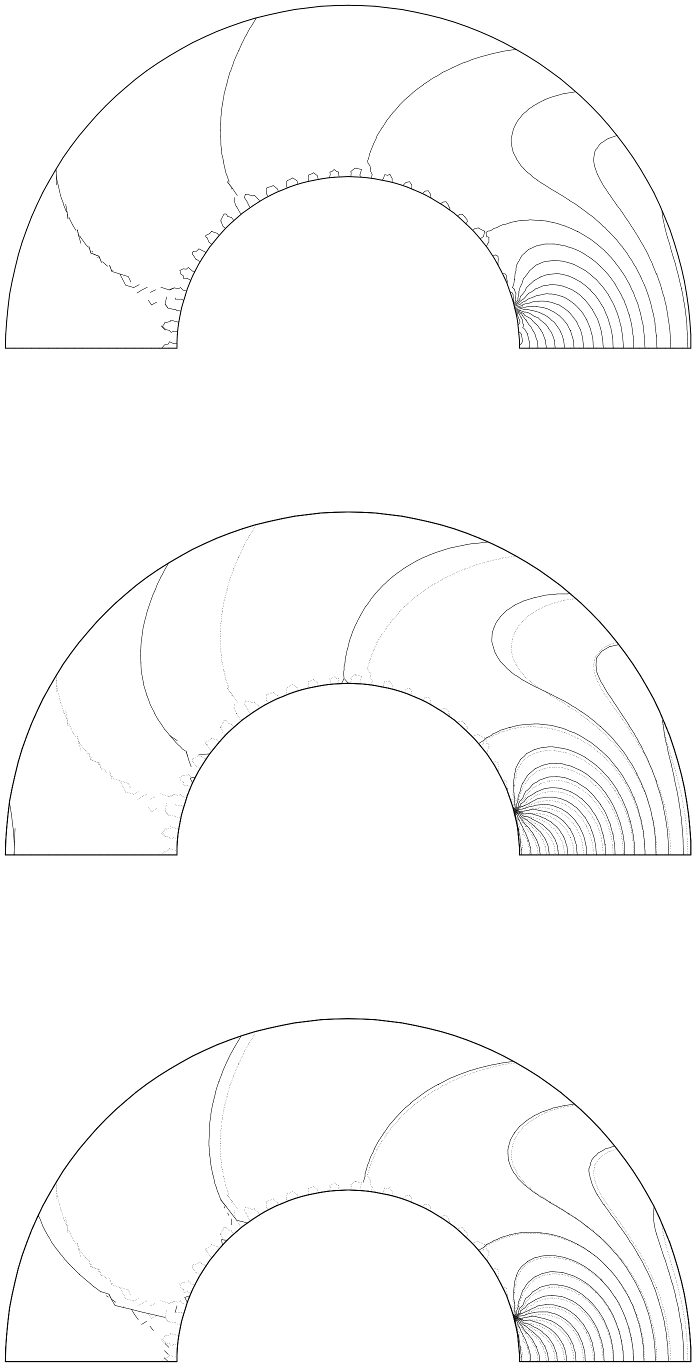

Figure 6.12: Solution contours for radiating element on a circular cylinder: (Top): Analytic series solution (50 terms) at time $t = 30$ and normalized frequency $ka = 3$. Space-time solution with local boundary condition, (Middle): $\mathbb{S}_1$ (Bottom): $\mathbb{S}_2$ (dotted contours denote analytic solution)

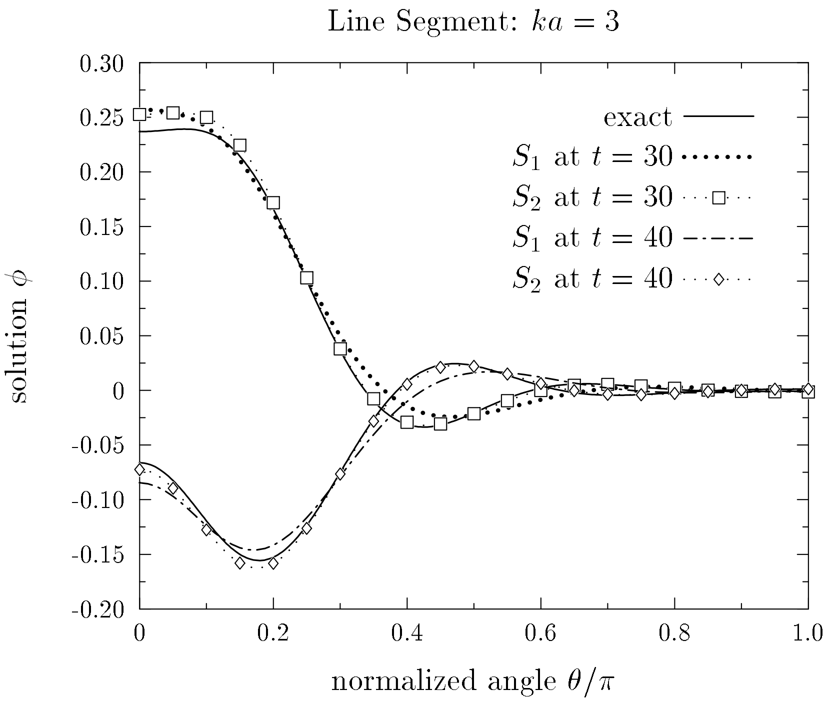

Figure 6.13: Radiating circular cylinder with line segment loading. Solution profile on the artificial boundary $r = R$.

$ka = 3$, nodally interpolated with the mesh employed. The low-amplitude oscillations in the vicinity of the inner boundary are a result of the difficulty the series solution has in resolving the discontinuity in the loading at $\theta_p = 13.5^o$, and are not relevant to the validation of the numerical results. Near $\theta = 0$, solutions using either the boundary condition $\mathbb{S}_1$ or $\mathbb{S}_2$ accurately capture the physics of the problem while as the wave spreads to the backside of the cylinder at $\theta = 180^o$, the solution using $\mathbb{S}_1$ deteriorates significantly while $\mathbb{S}_2$ maintains an accurate solution in this difficult region. These results are quantified in Figure 6.13, as a profile of the solution on Γ_∞ at $r = R$. Results from this and the previous example show the significant improvement in the numerical solution using the second-order operators $\mathbb{S}_2$, in comparison to the numerical solution using the operators $\mathbb{S}_1$ or $\mathbb{S}_0$.

6.6 Numerical Examples: Scattering

In this section numerical simulations of transient scattering from geometrically complex shapes are performed in order to demonstrate the effectiveness of the time-discontinuous Galerkin space-time finite element method to model multi-dimensional wave phenomena. In the following examples, use is made of the second-order local non-reflecting boundary condition $\mathbb{S}_2$ defined in (6.32). GLS mesh parameters are set to zero and quadratic space-time finite elements are used throughout.

6.6.1 Transient scattering from a circular cylinder

For this first example, consider the time-dependent scattering from an infinite circular cylinder of radius $r = a$. In the upper left corner of Figure 6.14 the finite element spatial discretization of the computational domain $\Omega = \{a \leq r \leq R, \, 0 \leq \theta \leq 2\pi\}$ bounded internally by the projection of the infinite circular cylinder, and externally by a circular artificial boundary with radius $R = 3a$ is shown. By symmetry only half the problem is modeled with 1200 quadratic elements. An incident pulse of short duration is generated by an acoustic source positioned midway between the cylinder and the circular artificial boundary, Γ_∞. This example represents a challenging problem where both the incident wave pulse and scattered waves should be transmitted through Γ_∞ with negligible reflection.

For this two-dimensional problem, the second-order local boundary condition defined in (6.32) is prescribed on Γ_∞. The source $f = \delta(x_0, y_0) \sin \omega t$ and $t \in [0\,,\,0.5]$, is positioned inside the computational domain at $(x_0, y_0) = (2a, 0)$, simulating an incident wave during a short time period. Setting the phase speed at $c = 1$ and frequency $\omega = 2\pi$ results in a challenging initial condition. The numerical simulation is continued until just prior to reaching the practical disappearance of the signal from the computational domain.

The numerical simulation at the end of the initial pulse is shown in Figure 6.14 at $t = 0.5$. The subsequent figures show the contours of the scattering phenomena with homogeneous Dirichlet boundary conditions on the cylinder surface $r = a$, i.e. 'release' boundary conditions. The following sequence of events occur:

- At $t = 1.5$ the incident pulse has expanded in a cylindrical wave and has just begun to reflect off the surface of the inner cylinder, while at the artificial boundary, the wave front passes through the boundary with no observable reflection.

- At $t = 2.5$ the incident wave continuous to diffract around the cylinder, creating a backscattered cylindrical wave that moves to the right and passes through the wake of the incident wave.
- At $t = 3.0$ the backscattered wave has just reached the artificial boundary.
- At $t = 4.0$ the backscattered wave is also transmitted through the artificial boundary with no observable reflection.

As a result of the homogeneous Dirichlet boundary conditions, the contours near the wet surface lie parallel to the cylinder outline and the amplitude of the backscattered wave is negative. Figure 6.15(top) shows the transient solution on the artificial boundary at the point $(r\,,\,\theta) = (R\,,\,0)$, for the case of homogeneous Dirichlet ('release') boundary conditions at the inner cylinder. Prior to time $t = 1$, the initial pulse has not reached the boundary Γ_∞ as indicated by the quiescent solution. Upon arrival at time $t = 1$, the solution advances as a sharp pulse with a wake of decaying amplitude. At time $t = 2.5$, the backscattered wave reaches Γ_∞, as indicated by pulse of negative amplitude.

For comparison, Figure 6.15(bottom) shows the transient solution when the boundary condition at the inner cylinder is changed to a homogeneous Neumann condition, i.e. a 'rigid' boundary condition. In this case the backscattered wave takes a positive amplitude.

6.6.2 Transient scattering from a square cylinder

In the next example consider the time-dependent scattering from an infinite square cylinder of dimension $a \times a$. The finite element spatial discretization for this problem is shown in Figure 6.16. By symmetry only the upper half is modeled with 1386 quadratic elements. The source $f = \delta(x_0, y_0)\sin\omega t$ and $t \in [0, 0.5]$, is prescribed with the same data and positioning as the previous example.

The numerical solution at the end of the initial pulse is shown in Figure 6.17 at $t = 0.5$. The sequence of events parallels the previous example: At $t = 1.5$ the incident pulse has expanded in a cylindrical wave and has just reached the vertex of the square

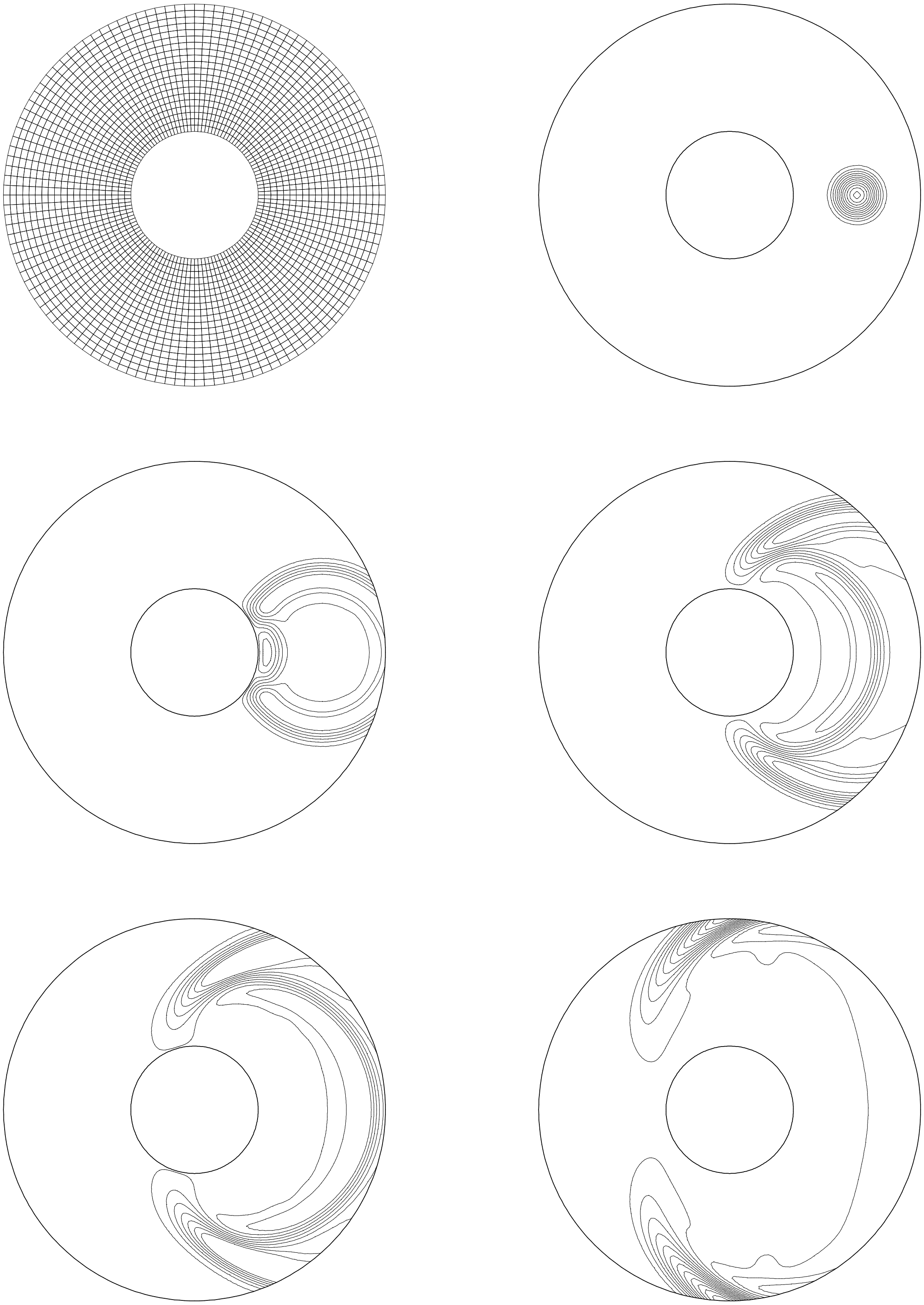

Figure 6.14: Scattering from an infinite circular cylinder due to point source. Solution contours shown at the end of the initial pulse at $t = 0.5$ and later times $t = 1.5$, $t = 2.5$, $t = 3$, and $t = 4$.

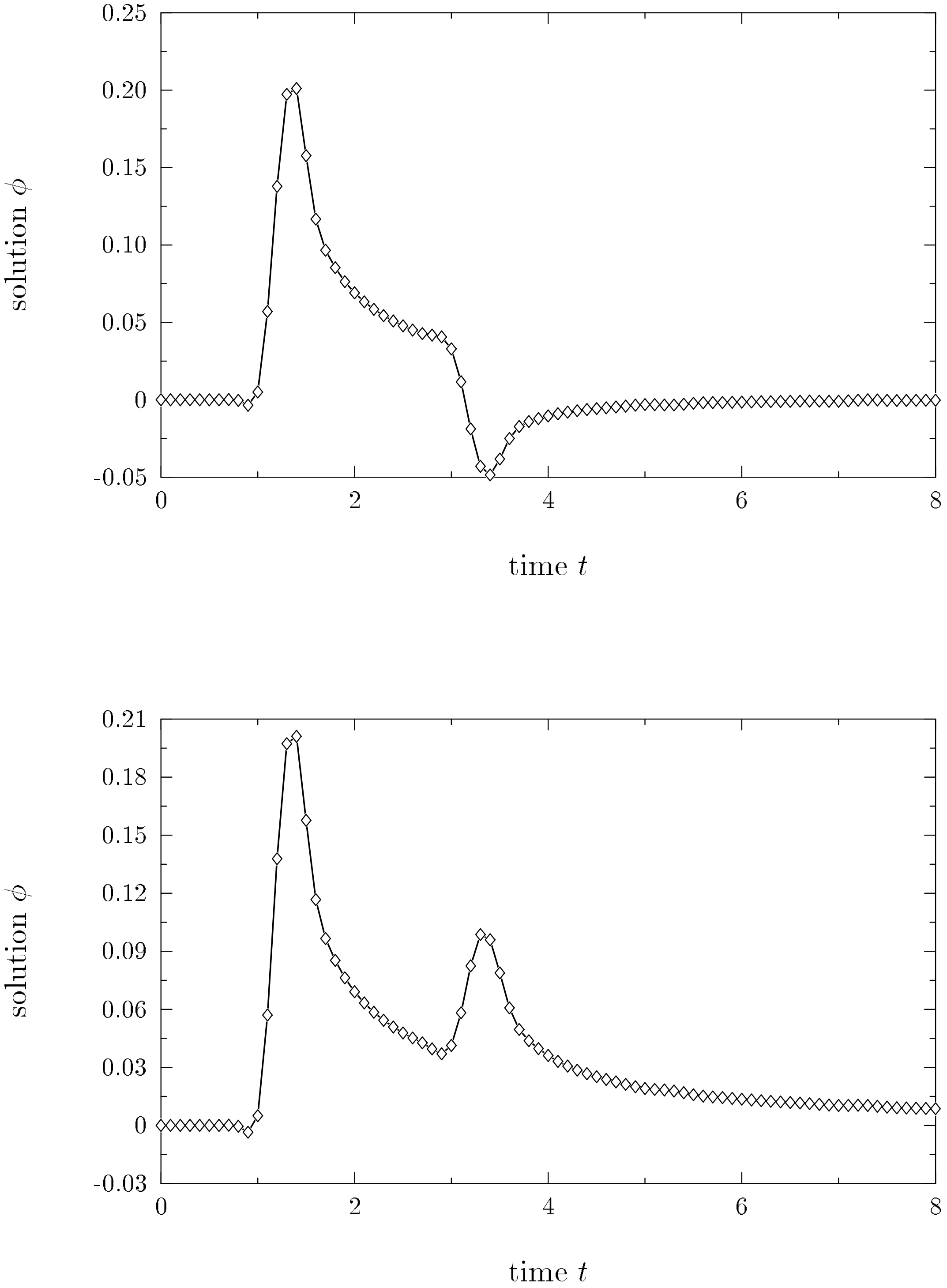

Figure 6.15: Scattering from an infinite circular cylinder: Solution on the artificial boundary Γ_∞, at $\theta = 0$. (top) 'pressure release' cylinder. (bottom) 'rigid' cylinder.

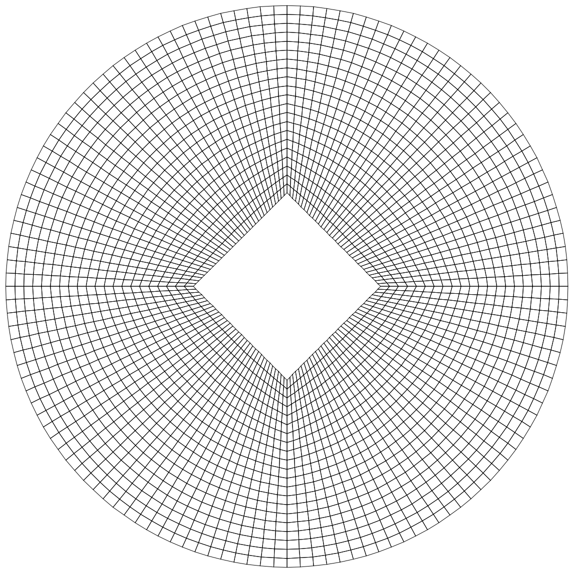

Figure 6.16: Spatial discretization for infinite square cylinder problem: By symmetry only upper half is modeled with 1386 quadratic elements.

scatterer. At $t = 2.5$ through $t = 3.0$ the incident wave has begun to reflect off the 'release' boundary, creating a backscattered wave. As time passes, both the incident and reflected waves are absorbed through the artificial boundary with no observable reflection. Figure 6.18 shows the transient solution on the artificial boundary Γ_∞, at $\theta = 0$, for both 'release' and 'rigid' boundary conditions on the square surface. Comparing these results to those found for the circular cylinder, we find that as a result of increased geometrical spreading, the amplitude of the backscattered wave is reduced while its duration is enlarged. 5

6.6.3 Transient scattering from a cylinder with end caps

Consider the time-dependent scattering from a rigid cylinder with conical-to-spherical end caps and a large length to diameter ratio, $L/d = 6.1$. Figure 6.20 illustrates the finite element spatial discretization of the computational domain. A total of 1600 quadratic elements are used for this example.

For this problem, the source $f = \delta(x_0, y_0) \sin \omega t$ and time $t \in [0, 3]$, is positioned

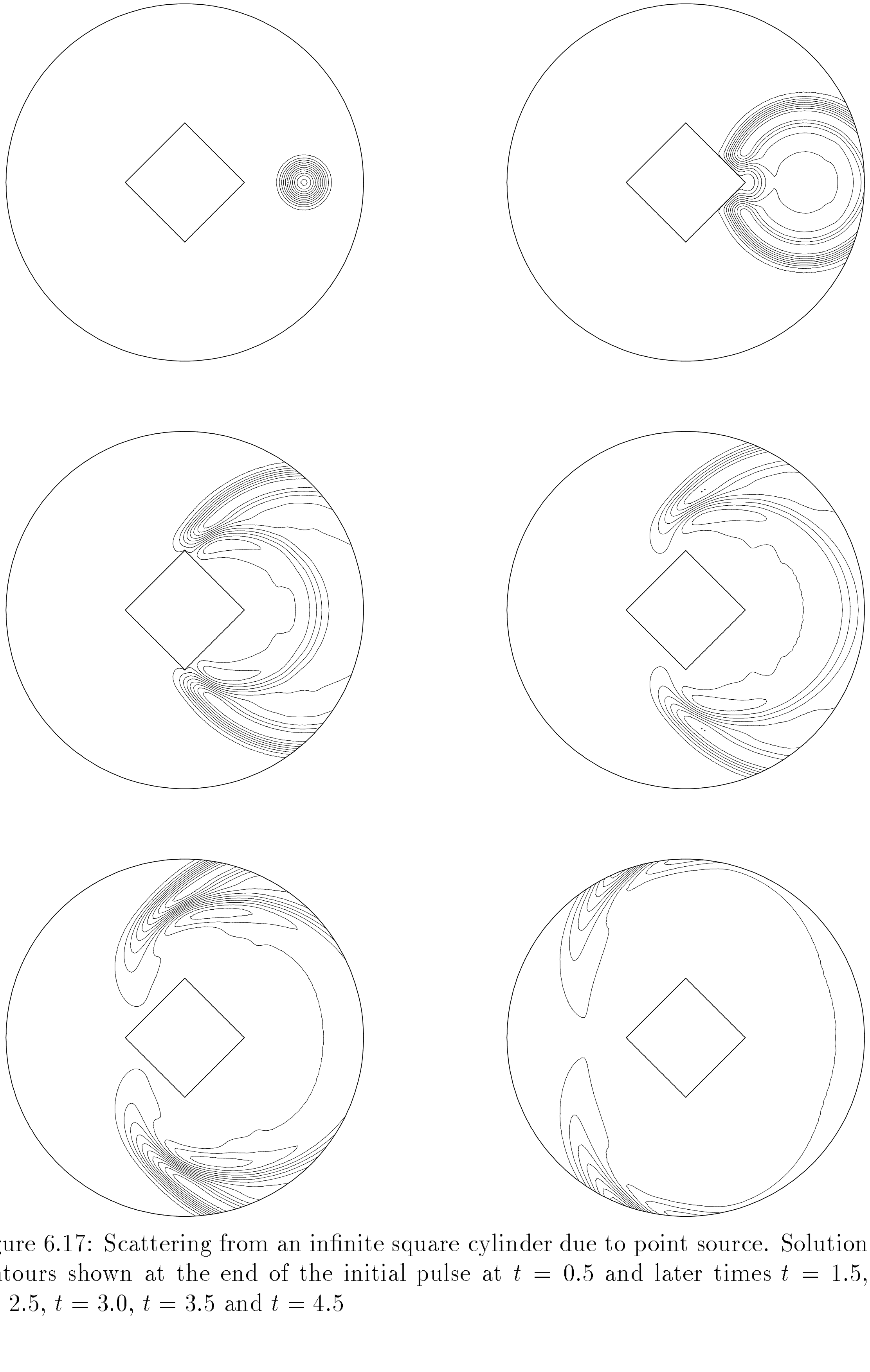

Figure 6.17: Scattering from an infinite square cylinder due to point source. Solution contours shown at the end of the initial pulse at $t = 0.5$ and later times $t = 1.5$, $t = 2.5$, $t = 3.0$, $t = 3.5$ and $t = 4.5$

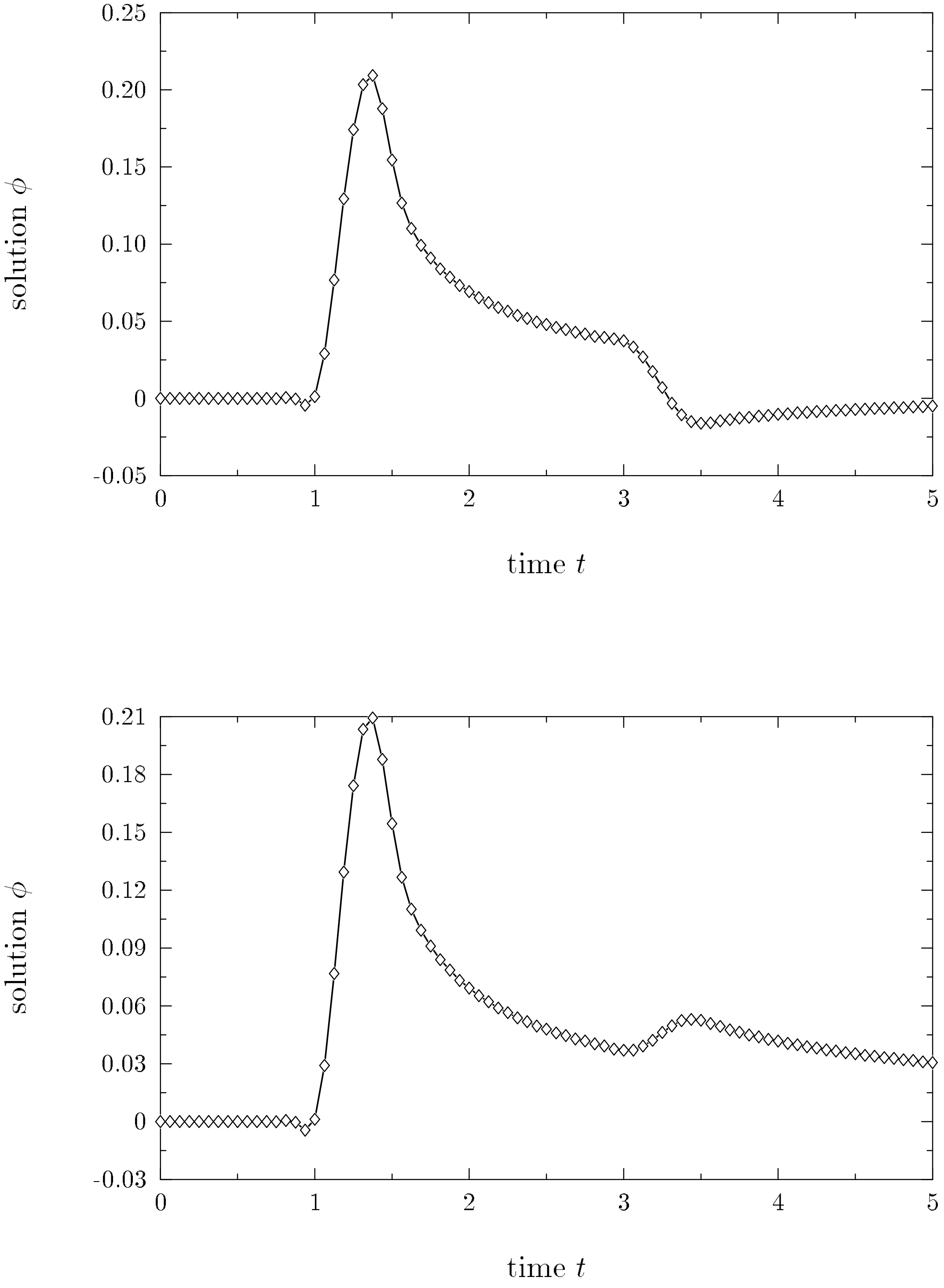

Figure 6.18: Scattering from an infinite square cylinder: Solution on the artificial boundary Γ_∞, at $\theta = 0$. (top) 'release' cylinder. (bottom) 'rigid' cylinder.

inside the computational domain simulating an oblique incident wave during a short time period. The phase speed is set at $c = 1$ with frequency $\omega = \pi/3$. In order to simulate an infinite structural impedance, homogeneous Neumann boundary conditions, i.e. 'rigid' boundary conditions, are prescribed on the cylinder surface. This example represents a challenging problem where the multiple-scales involving the ratio of the wavelength to diameter and length dimension play a critical role in the complexity of the resulting scattered wave field.

The numerical simulation at the end of the initial pulse at $t = 3$ is shown in Figure 6.20. The subsequent figures show the contours of the scattering phenomena as time progresses. The solution is presented in terms of the scalar velocity potential ϕ: Results for other solution variables such as the acoustic pressure $p = -\rho_0 \dot{\phi}$, or the acoustic velocity vector $\boldsymbol{v} = \nabla\phi$, are obtained through simple calculations of the time derivative and gradient of the velocity potential. The following sequence of events occur:

- At $t = 6$ the incident pulse has expanded in a cylindrical wave and has just reached the surface of the rigid cylinder, while at the artificial boundary, the wave front passes through the boundary with negligible reflection.

- At $t = 9$ through $t = 12$, the incident wave has begun to reflect off the cylinder boundary, creating a complicated backscattered wave.

- At $t = 15$, the incident wave begins to scatter into a part that travels along the upper part of the cylinder, and a part that diffracts around the backside. The backscattered wave is seen to transmit through the radiation boundary with no observable reflection.

- At $t = 18$, the incident wave has passed over the cylinder and continues to be absorbed through the non-reflecting boundary. A quiescent state near the right of the cylinder suggests the effectiveness of the local boundary condition in absorbing outgoing waves.

Note that as a result of the prescribed homogeneous Neumann boundary conditions on the cylinder, the amplitude of the reflected wave is positive creating high intensity zones in areas where the incident and backscattered waves coincide.

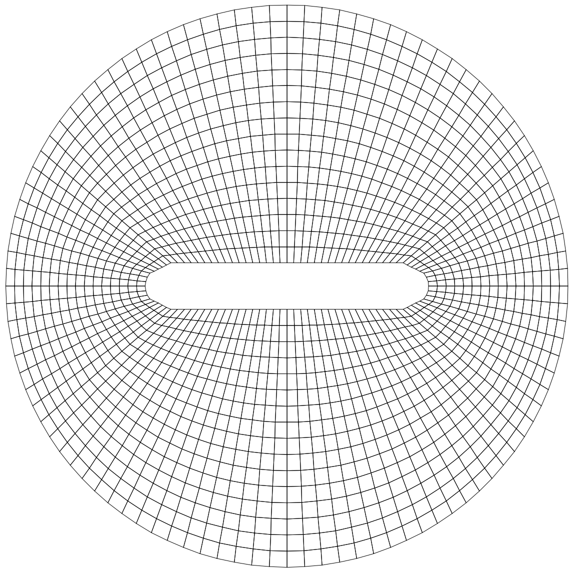

Figure 6.19: Spatial discretization for cylinder with tapered end caps. (1600 quadratic elements)

As a final example, consider the time-dependent scattering from the same cylinder described in Figure 6.19, but now with homogeneous Dirichlet boundary conditions on the wet cylinder surface, i.e. 'release' boundary conditions. The numerical simulation at the end of the initial pulse is shown in Figure 6.21 at $t = 3$. The sequence of events parallels the previous example: At $t = 6$ the incident pulse has expanded in a cylindrical wave and has just reached the boundaries of the cylinder. At $t = 9$ through $t = 12$, the wave has begun to reflect off the 'release' boundary, creating a complicated backscattered wave. As time passes, the originally cylindrical incident wave begins to scatter into a part that travels along the upper part of the cylinder, and a part that diffracts around the backside. The backscattered wave is seen to transmit through the boundary with no observable reflection. Note that as a result of homogeneous Dirichlet boundary conditions, the contours lying near the wet surface are parallel to the cylinder and the amplitude of the backscattered wave is negative.

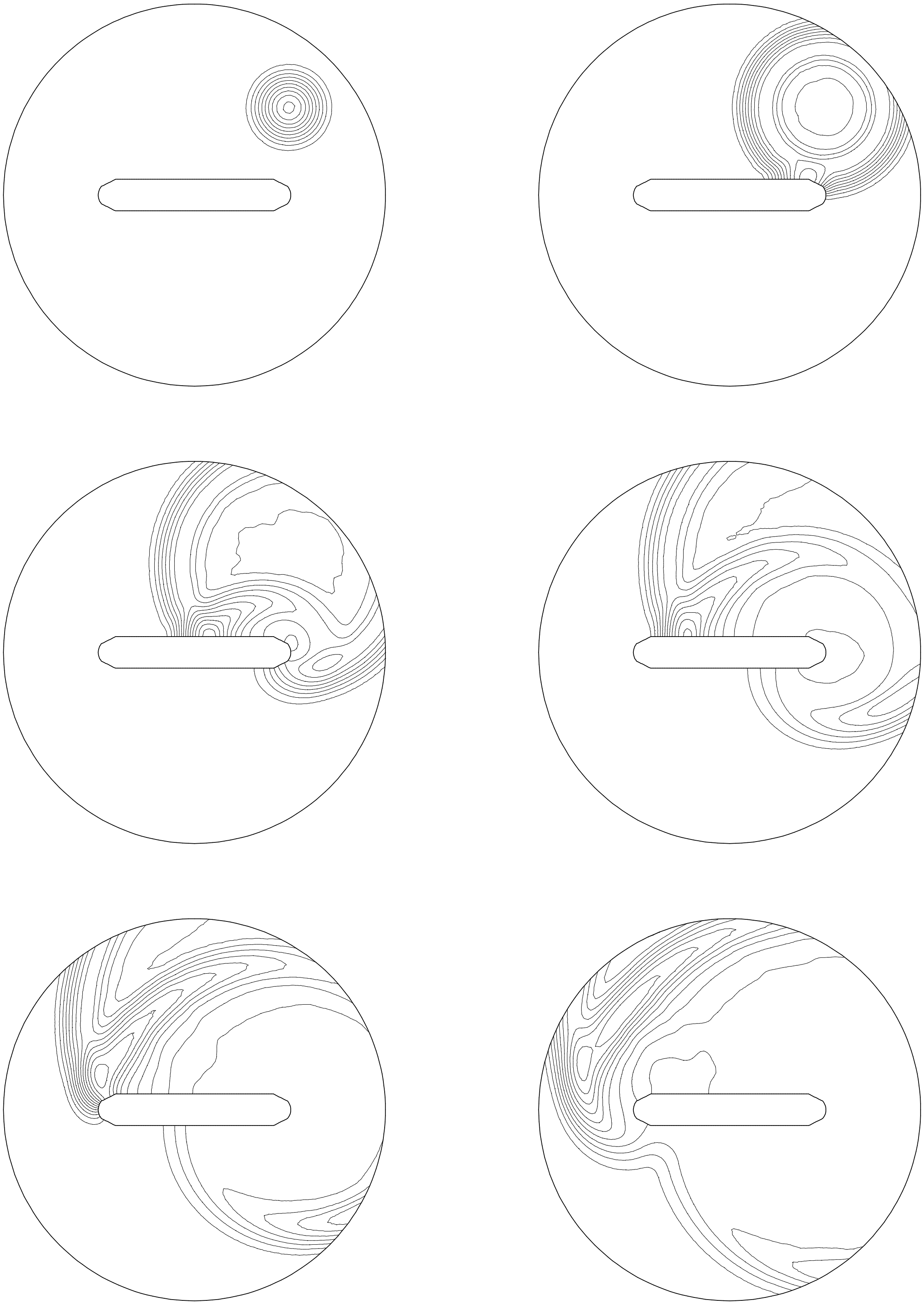

Figure 6.20: Scattering from a 'rigid' cylinder with tapered end caps due to point source. Solution contours shown at the end of the initial pulse at $t = 3$ and later times $t = 6, 9, 12, 15, 18$.

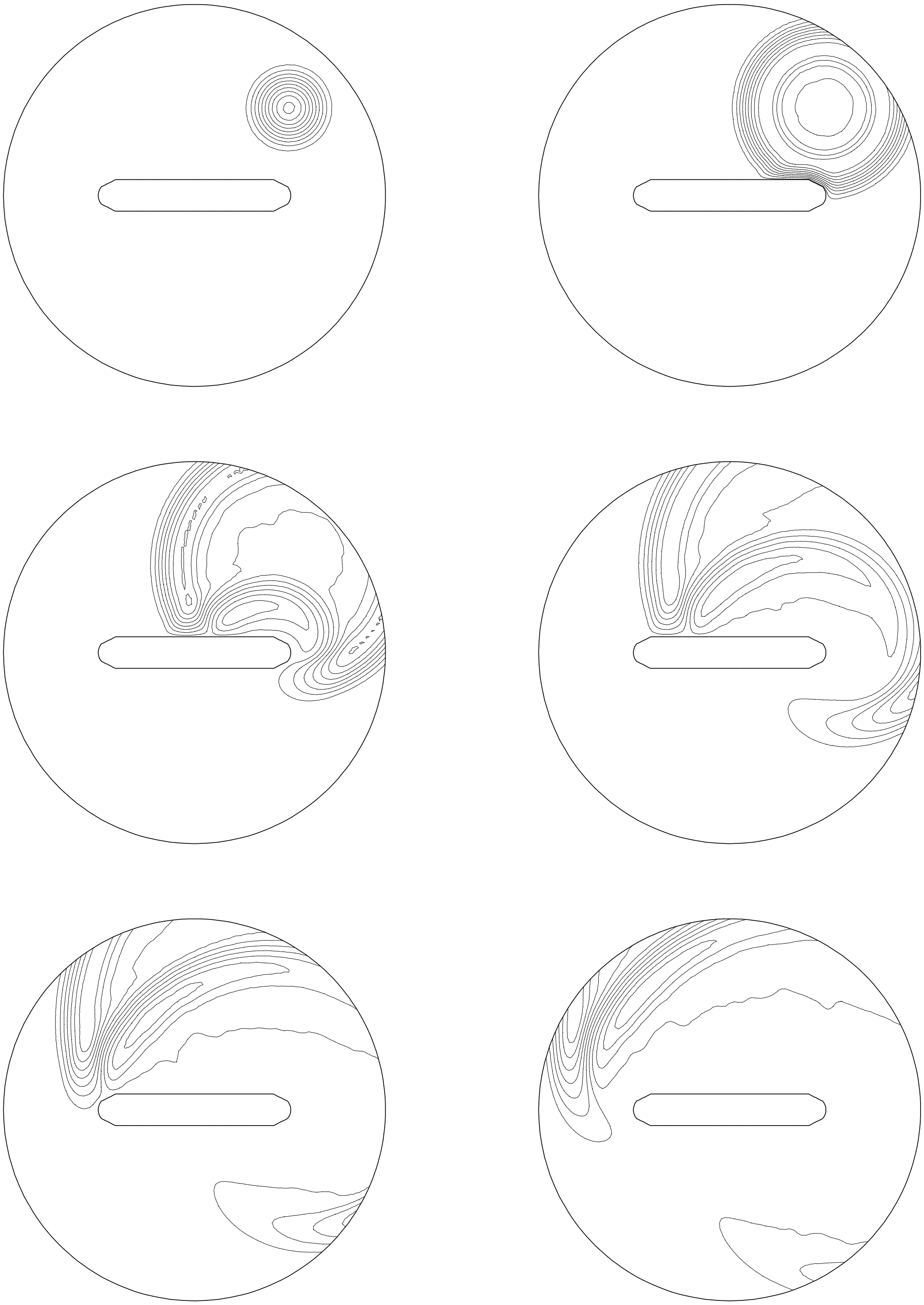

Figure 6.21: Scattering from a 'release' cylinder with tapered end caps due to point source. Solution contours shown at the end of the initial pulse at $t = 3$ and later times $t = 6, 9, 12, 15$ and $t = 18$.

6.7 Summary and Conclusions

For the two-dimensional problem, it is not possible to obtain local time-dependent boundary conditions that exactly represent outgoing cylindrical wave harmonics on the artificial boundary. The difficulty can be traced to the representation of cylindrical Hankel functions appearing in the wave harmonics for the exact solution in the frequency domain. Because of this difficulty, we resort to an approximation to the exact solution for outgoing waves expressed as an asymptotic expansion for large frequency (short wavelength), normalized with the radius of the circular artificial boundary. It has been demonstrated that this radially asymptotic expansion can be obtained starting from the exact Dirichlet-to-Neumann map.

Following Bayliss and Turkel [1980,82] a sequence of differential operators are defined which match the leading terms of the asymptotic approximation to provide local boundary conditions which are of progressively higher order and increasing accuracy. These boundary operators have an inverse Fourier transform allowing a family of boundary conditions that are local in space and time. Since the non-reflecting boundary conditions are local in space and time they preserve the data structure of the space-time finite element method for any order m. After eliminating higher-order radial derivatives through the use of the wave equation, this sequence of non-reflecting boundary conditions can easily be incorporated into the time-discontinuous space-time finite element method.

Numerical results confirm the superiority of the second-order local non-reflecting boundary condition $\mathbb{S}_2$, in comparison to the first-order $\mathbb{S}_1$, and simple 'plane-wave' $\mathbb{S}_0$, operators. The examples in this chapter demonstrate that with proper usage, the second-order non-reflecting boundary condition $\mathbb{S}_2$, when implemented in the space-time finite element method, is sufficiently accurate to capture all the important physics associated with a variety of complicated transient scattering problems.

An area of great potential for space-time finite element methods when solving time-dependent scattering problems, is the development of effective adaptive mesh refinement/unrefinement strategies in both space and time. This is especially important where both temporal and spatial enhancement can occur to track wave fronts as they propagate over large distances and long time intervals. For the examples given in this thesis, the full potential of the discontinuous space-time finite element method was not exploited in that a uniform mesh was fixed at each time step. JOHNSON [1993] and colleagues have recently developed some *a posteriori* error estimates for the discontinuous Galerkin method useful for developing adaptive strategies for the second-order hyperbolic wave equation. Further research efforts are needed to develop efficient and accurate local error indicators to drive the implementation of adaptive strategies for the exterior structural acoustics problem incorporating non-reflecting boundaries. For transient problems where waves propagate throughout the computational domain as a 'local' signal of relatively short duration, e.g. the scattering examples given in the previous section, adaptive methods should be able to reduce solution costs significantly. This may be accomplished by adding extra degrees of freedom in regions local to the signal, and deleting degrees of freedom in areas that are relatively quiescent.